

# Compaction of granular material inside confined geometries

Benjy Marks<sup>1,2\*</sup>, Bjørnar Sandnes<sup>2</sup>, Guillaume Dumazer<sup>1</sup>, Jon A. Eriksen<sup>1,3</sup> and Knut J. Måløy<sup>1</sup>

<sup>1</sup> Condensed Matter Physics, Department of Physics, University of Oslo, Oslo, Norway, <sup>2</sup> College of Engineering, Swansea University, Swansea, UK, <sup>3</sup> Centre National de la Recherche Scientifique, Institut de Physique du Globe de Strasbourg, University of Strasbourg/Ecole et Observatoire des Sciences de la Terre, Strasbourg, France

## OPEN ACCESS

### Edited by:

Daniel Bonamy,  
Commissariat à l'Énergie Atomique et  
aux Énergies Alternatives, France

### Reviewed by:

Eric Josef Ribeiro Parteli,  
University of Erlangen-Nuremberg,  
Germany  
Ferenc Kun,  
University of Debrecen, Hungary

### \*Correspondence:

Benjy Marks,  
Condensed Matter Physics,  
Department of Physics, University of  
Oslo, Sem Sælands Vei 24,  
Fysikkbygningen, Oslo 0371, Norway  
benjy.marks@fys.uio.no

### Specialty section:

This article was submitted to  
Interdisciplinary Physics,  
a section of the journal  
Frontiers in Physics

**Received:** 20 April 2015

**Accepted:** 27 May 2015

**Published:** 09 June 2015

### Citation:

Marks B, Sandnes B, Dumazer G,  
Eriksen JA and Måløy KJ (2015)  
Compaction of granular material inside  
confined geometries.  
Front. Phys. 3:41.  
doi: 10.3389/fphy.2015.00041

In both nature and engineering, loosely packed granular materials are often compacted inside confined geometries. Here, we explore such behavior in a quasi-two dimensional geometry, where parallel rigid walls provide the confinement. We use the discrete element method to investigate the stress distribution developed within the granular packing as a result of compaction due to the displacement of a rigid piston. We observe that the stress within the packing increases exponentially with the length of accumulated grains, and show an extension to current analytic models which fits the measured stress. The micromechanical behavior is studied for a range of system parameters, and the limitations of existing analytic models are described. In particular, we show the smallest sized systems which can be treated using existing models. Additionally, the effects of increasing piston rate, and variations of the initial packing fraction, are described.

**Keywords:** granular material, Janssen stress, boundary effects, confinement, deformable media, hele-shaw cell, discrete element method, micromechanics

## 1. Introduction

When granular materials are placed in confined geometries, we often observe a significant portion of the stress being redirected toward the confining boundaries. This phenomenon has been systematically studied for many systems [1–3], most notably in silos, beginning with Janssen [4]. Force redirection has been attributed to the granular nature of the material, and has in many cases been shown to be well represented by a constant coefficient, known as the Janssen coefficient  $K$ , defined in one spatial dimension as

$$K = \sigma_r / \sigma_n,$$

where  $\sigma_r$  is the redirected stress due to some applied normal stress  $\sigma_n$ . Here we investigate the development of stresses within a granular packing, confined vertically between two horizontal plates, with no walls in the remaining directions, subjected to a rigid piston impacting it from one side. As the piston moves, granular material is compacted near the piston, and with increasing displacement of the piston, the size of the packing increases. Such an accumulation process is known to occur in the petroleum industry, where sand is liberated from the host rock during extraction, altering the underground morphology of cracks [5, 6]. This may also be relevant for understanding proppant flowback in propped fractures [7]. Additionally, this geometry is representative of a number of recent experimental studies in Hele-Shaw cells [8–11] where the validity of Janssen stress redirection has not been ascertained.

There are a number of interesting patterns which form when a granular material is displaced by a flexible interface in such a geometry [9, 11]. The nature of the patterns have been shown to depend on many factors, primarily the initial packing fraction and the rate of displacement [10]. For this reason, we here investigate the microstructural and mechanical evolution of such a system under these conditions. To reduce the complexity of the system, we consider only a rigid piston.

We are interested in systems which are highly confined. In common experiments with granular material inside Hele-Shaw cells, there are in general fewer than 20 grain diameters between the two Hele-Shaw plates, typically down to around 5 grain diameters [10]. As the confinement increases, i.e., as the gap spacing decreases, we expect a transition from three dimensional behavior toward a behavior governed by the boundaries, as demonstrated for vertical silos in Bratberg et al. [12]. It is then of interest to study the changes that result from increasing confinement. We expect that altering the confinement will affect the force redistribution. A transition may occur for extremely confined systems where such an assumption concerning force redirection may not be valid.

Existing analytic models for the micromechanics of such a system generally reduce the problem to one spatial dimension ( $x$ ), assuming that variations in both remaining directions ( $y$  and  $z$ ) are small, although recently curved interfaces have also been described [8]. For simplicity, we consider a flat interface, and validate the analytic description with a discrete element model.

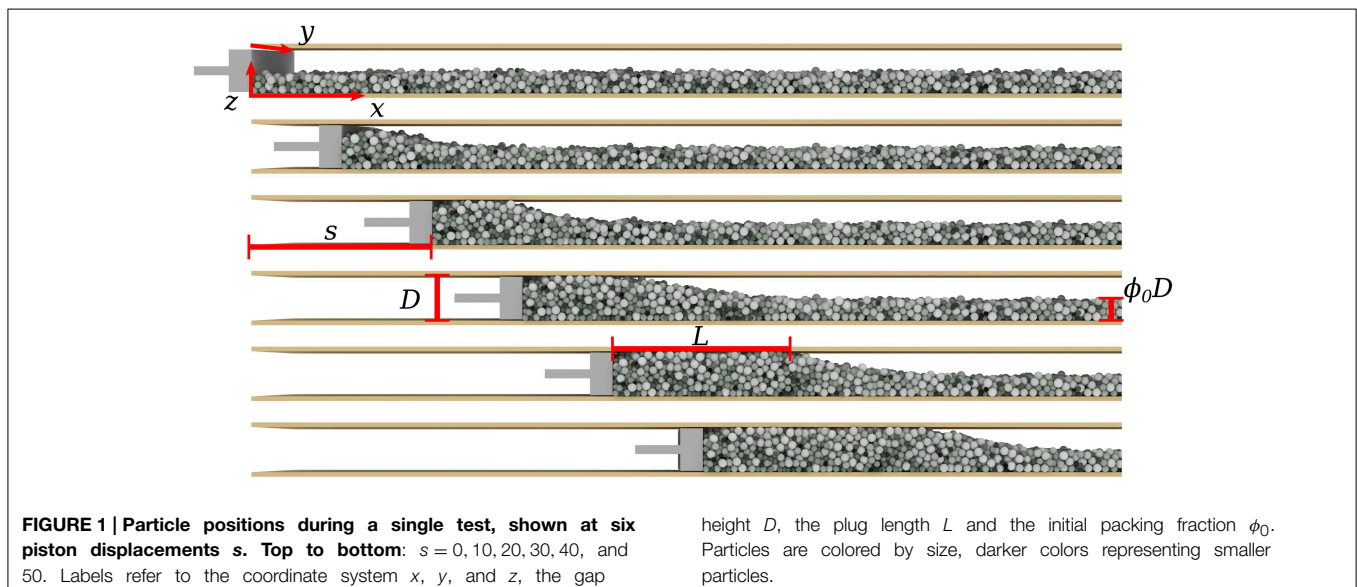
Firstly, in Section 2 describe the numerical model that has been used to simulate this system. In Section 3, we establish continuum properties which correspond to the analytic formulation, and show comparisons between the two. In particular, the limitations of current analytic models are identified. Finally, a parameter set is proposed that best fits the analytic theories for a wide range of system variables.

## 2. Materials and Methods

This paper is an investigation into the micromechanics of a system which is highly constrained by external boundaries. For this reason, it is ideal to use a particle based method to model the behavior, as the total number of grains in the system is small. Toward this end, we use a conventional soft sphere discrete particle approach, implemented in the open source code MercuryDPM ([www.mercurydpm.org](http://www.mercurydpm.org)) [13, 14]. The geometry considered here, shown in **Figure 1**, consists of a rigid piston, oriented in a space  $r = \{x, y, z\}$ , with normal along the  $x$  axis, which pushes particles between two rigid plates, separated by a spacing  $D$  and having normals in the  $\pm z$  directions, with two periodic boundaries in the remaining perpendicular direction,  $y$ . The coordinate system moves with the piston, such that it is located at  $x = 0$  at all times. As the piston moves horizontally at a velocity  $u$  toward the grains, its displacement at any time  $t$  is then  $s = ut$ .

We work in a system of non-dimensionalized units with the following properties; length and mass have been non-dimensionalized by the length  $d'_m$  and mass  $m'_m$  of the largest particle in the system, respectively, where the prime indicates that the quantity has dimension. The particle diameters,  $d$ , we use are therefore  $d \leq 1$ , with material density defined by  $4\pi(1/2)^3\rho_p/3 = 1$ , or  $\rho_p = 6/\pi$ . Time is non-dimensionalized by the time taken for the largest particle to fall from rest its own radius under the action of gravity, so that a unit time is  $t = \sqrt{d_m/g}$ , which requires that  $g = 1$ . Other values are non-dimensionalized by a combination of these three scales, for example stress is non-dimensionalized by  $m'_m g' / d_m'^2$ .

Particles are filled into the available space by assigning them to positions on a regular hexagonally close packed lattice, dimensioned such that particles of diameter 1 would be in contact. In all cases we use particles distributed uniformly in the range  $0.5 \leq d \leq 1$  to avoid crystallization, and to mimic the size range used in Sandnes et al. [10]. Variable particle filling is



facilitated by changing the number of layers of the grid, such that the initial packing fraction,  $\phi_0$  defined in Equation (3), is approximately constant throughout the cell. From  $t = -10$  to  $t = 0$ , gravity in the  $-z$  direction is increased from  $g = 0$  to  $g = 1$  to settle the grains in a loose packing. From  $t = 0$  the piston begins to move at velocity  $u$ .

As shown in **Figure 2**, the particles' material properties are described by normal, tangential and rolling damped spring sliders [13, 15] with the properties contained in **Table 1**. These values have previously been calibrated to mimic 20 micron silica beads [16]. Here we neglect the role of adhesion between particles, which will become increasingly important as the physical size of the particles reduces. The walls are implemented such that they are rough; when a particle contacts a wall, the piston, or both, it is prohibited from rotating, i.e.,  $\mu_r = 1$ . Otherwise, the interaction properties are the same as between two particles, except that the walls and piston are of infinite mass. We therefore have a well defined macroscopic sliding friction of  $\mu = 0.4$  that does not depend on the rate of loading.

In the following Section we will firstly detail the important macroscopic quantities measured from a single simulation. We will then investigate the effect of three controlling parameters on the evolution of the system: the Hele-Shaw spacing  $D$ , the initial packing fraction  $\phi_0$  and the velocity of the piston,  $u$ . The piston

rate, however, is not *a priori* a governing quantity, so we choose to control the piston rate via the inertial number,  $I$ , which is defined as  $I = \dot{\gamma} d_m / \sqrt{P/\rho_p}$ , which is the ratio of inertial to imposed stresses, where  $P$  is a typical pressure and  $\dot{\gamma}$  is a typical shear strain rate [17]. Taking  $\dot{\gamma} = u/D$ , and  $P = \rho_p g D$ , gives

$$I = \frac{u d_m}{D^{3/2} g^{1/2}} = u D^{-3/2}.$$

### 3. Results

As depicted in **Figure 1**, three distinct regions exist inside the system. These are termed the *plug zone*, where particles are densely packed near to the piston ( $x \leq L$ ), the *undisturbed zone*, far from the plug, and the *transition zone*, where the plug is accumulating. To define these regions systematically, we must first measure the solid fraction,  $v = V_s/V_t$ , which is a local measure of the ratio of the volume of solids to the total volume. The solid fraction is coarse grained in one spatial dimension,  $x$ , as

$$v(x, t) = \frac{1}{WD} \sum_{i=1}^N V_i \mathcal{W}(x - x_i(t)), \quad (1)$$

where  $N$  is the number of grains in the system,  $W$  is the width of the system,  $V_i$  is the volume of the  $i$ -th grain,  $x_i$  its center of mass and  $\mathcal{W}$  is the coarse graining function, chosen in this case to be a 1D normalized Gaussian function [14, 18]. Such a coarse graining method allows the coarse graining width to be defined, so that either the macro- or micro-structure is visible. We choose to use a coarse graining width equal to the maximum particle diameter, such that small scale variations are minimized, and smooth continuum fields are obtained [19]. All other continuum quantities are defined using the same coarse graining technique, presented in Goldhirsch [18], Weinhart et al. [14]. Using the definition (1), we denote the maximum solid fraction,  $v_m$ , as an average over the solid fraction close to the wall at some time when the transition zone is far from the piston as

$$v_m = \frac{1}{5D} \int_{5D}^{10D} v(x) dx, \quad (2)$$

where in practice a numerical integration is done over the discrete coarse grained cells, and the limits of  $5D$  and  $10D$  are chosen arbitrarily. We define the normalized packing fraction,  $\phi(x, t)$ , as  $\phi = v/v_m$ , and note that in the absence of volumetric expansion or dilation of the granular material,  $\phi$  is directly proportional to the height of the packing between the Hele-Shaw walls. The undisturbed zone is that which is maintained at the initial packing fraction  $\phi_0$ , which is defined at time  $t = 0$  as

$$\phi_0 = \frac{1}{5D} \int_{5D}^{10D} \phi(x, t = 0) dx.$$

To delineate the plug, transition and undisturbed zones, at each time  $t$  we use linear regression to find the best linear fit to the

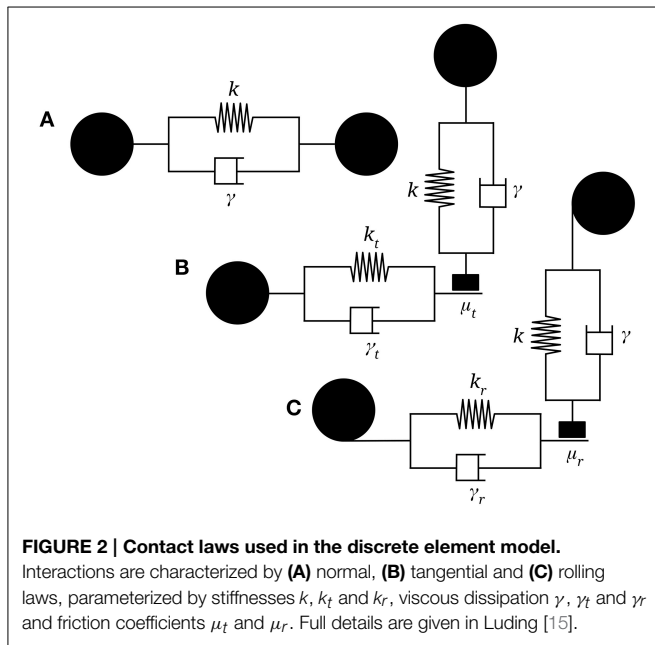


**TABLE 1 | Material properties of the spheres.**

Direction	Stiffness, $k$ $\left(\frac{\text{kg/s}^2}{m'_m/\sqrt{g'd'_m}}\right)$	Dissipation, $\gamma$ $\left(\frac{\text{kg/s}}{m'_m/\sqrt{g'd'_m}}\right)$	Coefficient of friction, $\mu$
Normal	1,00000	1000	-
Tangential	80,000	0	0.4
Rolling	80,000	0	$10^{-3}$

points in the range  $\phi = \phi_0 + 0.1$  to  $\phi = 0.9$ , such that  $\phi D \approx b - x \tan \theta$ , for some value of  $b$  and slope angle  $\theta$ . Five examples of this are shown in **Figure 3A**. Using this best fit, we can define the point at which the plug zone meets the transition zone as the intersection of the best fit regression line and  $\phi = 1$ , such that  $L = (b - D)/\tan \theta$ , as shown in **Figure 3A**. The value of  $L$  grows monotonically with piston displacement, as shown in **Figure 3B**. Conservation of mass implies that on average, if there is no volumetric change in the packing, and no slip between the grains and the walls, this relationship can be expressed as

$$\frac{L}{s} = \frac{\phi_0}{1 - \phi_0}, \quad (3)$$

which is shown as the dashed line in **Figure 3B**. For all cases reported here, the value of  $\theta$  does not appear to vary with increasing plug length  $L$ . The point at which the undisturbed zone meets the transition zone can then be defined in a similar manner as above, by the intersection of the

best fit regression line with  $\phi = \phi_0$ . The coordination number,  $Z$ , (average number of contacts per particle), is fairly constant in the plug zone, (**Figure 3C**), increasing with compaction, as rearrangement occurs. Additionally, at large values of  $L$  the stresses are high enough to cause significant overlap of the particles (up to 1%). In the transition zone, significant particle rearrangement lowers the coordination number.

Coarse graining techniques in general cause measured fields to converge toward zero near boundaries [14]. While it is feasible to reconstruct these fields in general near individual boundaries, near the piston we have three distinct boundaries which all interact. To access stresses in this region, it is then preferable to directly measure the forces applied to the rigid boundaries of the system. Toward this end, we denote  $\sigma_n^p$  as the normal stress measured at the piston. This is shown as a function of piston displacement in **Figure 3D**. The stresses measured from coarse graining within the packing are shown in **Figure 3E**. In both cases, the stresses grow exponentially both with increasing

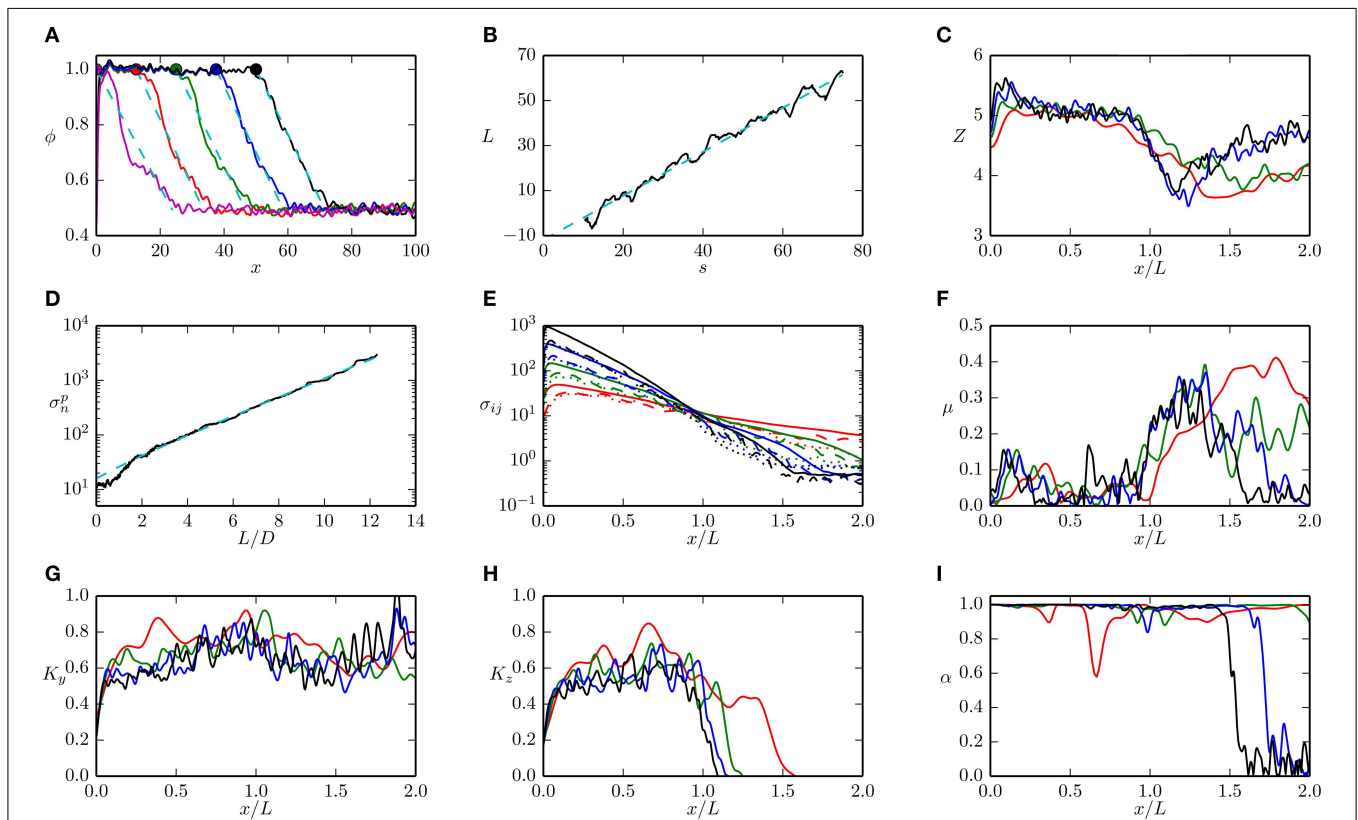


**FIGURE 3 | Evolution of coarse grained properties of the system with increasing piston displacement,  $s$ , for  $D = 5$ ,  $\phi_0 = 0.5$  and  $I = 0.01$ .** (A) Five examples of the normalized packing fraction of the particles,  $\phi$ . The magenta, red, green, blue, and black lines indicate displacements which correspond to  $L = 0, 12.5, 25, 37.5$ , and  $50$  respectively. The same color scheme is used for each subsequent plot in this Figure unless stated otherwise. A filled circle indicates the measured value of  $L$ , and the cyan dashed line indicates the linear best fit measurement of the transition zone. (B) Evolution of the measured value of  $L$  with increasing displacement  $s$  drawn in black. The cyan line

indicates the best linear fit to these points. (C) The coordination number,  $Z$ , as a function of normalized distance from the piston head,  $x/L$ . (D) Normal stress measured at the piston is shown in black. The cyan dashed line indicates the best fit estimate of Equation (6). (E) Normal stress distributions within the packing. Solid lines indicate  $\sigma_{xx}$ , dashed  $\sigma_{yy}$  and dotted  $\sigma_{zz}$ . (F) Apparent friction coefficient measured within the packing,  $\mu = |\sigma_{xz}|/\sigma_{zz}$ . (G) Out of plane Janssen coefficient measured within the packing,  $K_y = \sigma_{yy}/\sigma_{xx}$ . (H) In plane vertical Janssen coefficient measured within the packing,  $K_z = (\sigma_{zz} - \rho_p v g D/2)/\sigma_{xx}$ . (I) Absolute value of the  $x$  component of the eigenvector of the major principal stress.

$L$  and decreasing  $x$ , as shown by the linearity in a semilog space in **Figures 3D,E**.

An analytic expression to describe this stress evolution was first derived in Knudsen et al. [9], assuming that: (a) the stress redirection in the  $z$  direction is described by a constant  $K_z = \sigma'_{zz}/\sigma_{xx}$ , where  $\sigma'_{zz} = \sigma_{zz} - D\rho_p v_m g/2$  is the component of the vertical stress not due to gravity and (b) friction at the side walls is  $\mu = \sigma_{xy}/\sigma_{zz}$ . It can be shown using force balance in the  $x$  direction that under these conditions, if there is no net acceleration,

$$\frac{d\sigma_{xx}}{dx} = -\frac{2\mu K_z}{D}\sigma_{xx} - \mu\rho_p v_m g.$$

By further assuming that the stress at  $x = L$  is a constant, i.e.,  $\sigma_T \equiv \sigma_{xx}(x = L)$ ,

$$\sigma_{xx} = \left(\sigma_T + \frac{D\rho_p v_m g}{2K_z}\right) e^{2\mu K_z(L-x)/D} - \frac{D\rho_p v_m g}{2K_z}. \quad (4)$$

Previously, the threshold stress  $\sigma_T$  has been modeled as either estimated from experimental data [8], or as a constant by assuming sliding of a wedge of material [9, 11]. Here, we choose to model the threshold stress  $\sigma_T$  as a  $\phi_0$  dependent quantity by considering limit equilibrium of a wedge of material being displaced into the undisturbed zone, as shown in **Figure 4**. We assume a noncohesive Coulomb failure of the material internally, along a failure plane parallel to and meeting the surface of the transition zone. We additionally assume that the internal friction angle is also defined by  $\mu$ . Limit equilibrium in the  $x$  direction can then be expressed using the notation defined in **Figure 4** as  $F_x = T_b + T_i \cos \theta$ , where  $F_x = D\sigma_T$ ,  $T_b = \mu W_0 = \mu D^2 \rho_p v_m g / (2 \tan \theta)$  and  $T_i = \mu W_1 \cos \theta = \mu D^2 \rho_p v_m g \phi_0^2 \cos \theta / (2 \tan \theta)$  per unit length in the  $y$  direction. After some rearrangement this implies that

$$\sigma_T = \frac{\mu D \rho_p v_m g}{2 \tan \theta} (1 + \phi_0^2 \cos^2 \theta). \quad (5)$$

This assumption of the failure surface introduces no new parameters into the model, and as will be shown in the following, closely predicts the measured value of  $\sigma_T$  for a large range of system parameters. In the limit where  $\phi_0 \rightarrow 0$ , this definition

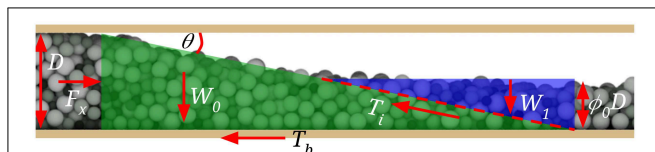


**FIGURE 4 | Limit equilibrium of the transition zone.** For the pile to be displaced by a force  $F_x$ , two forces must be overcome;  $T_b$ , the basal traction due to the weight  $W_0$  of the green region, and the  $x$  component of the internal sliding traction  $T_i$  along the assumed failure surface denoted by the dashed line, due to the normal component of the weight above the failure surface,  $W_1$ , of the blue region.

reduces to that used in Knudsen et al. [9] and Sandnes et al. [11]. Including this new definition of the threshold stress, Equation (5), in Equation (4) gives

$$\sigma_{xx} = \frac{D\rho_p v_m g}{2K_z} \left( \left( \frac{\mu K_z}{\tan \theta} (1 + \phi_0^2 \cos^2 \theta) + 1 \right) e^{2\mu K_z(L-x)/D} - 1 \right). \quad (6)$$

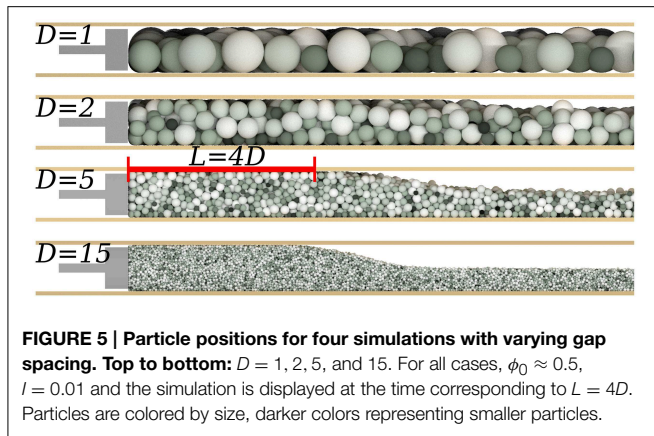
A best fit estimate is used to find  $K_z$  from Equation (6), and is shown as the dashed line in **Figure 3D** at  $x = 0$ , using the measured values of  $v_m$ ,  $\theta$  and  $\phi_0$ , which adequately captures the behavior of the system past  $L/D = 2$ . Before this limit, stress redistribution has not saturated, and  $\sigma_{xx}$  is less than the predicted value. We find the same transition value of  $L/D \approx 2$  for all cases reported here.

The measured value of apparent friction  $\mu = \sigma_{xz}/\sigma_{zz}$  inside the packing, shown in **Figure 3F** shows that the system is far from failure inside the plug zone, and increasingly unstable in the transition zone. The out of plane Janssen coefficient,  $K_y = \sigma_{yy}/\sigma_{xx}$ , shown in **Figure 3G**, has large variations in  $x$ , but is not significantly affected by the formation of the plug. The in plane Janssen coefficient (**Figure 3H**),  $K_z = \sigma'_{zz}/\sigma_{xx}$ , however, is strongly influenced by the formation of the plug, and is relatively constant with increasing  $L$  inside the plug zone.

An underlying assumption of the Janssen stress redistribution is that when averaging over the width of the system (here in the  $y$  and  $z$  directions), the principal stress directions are parallel to the system geometry [4]. For this reason we measure  $\alpha$ , the absolute value of the  $x$  component of the eigenvector of the major principal stress, which is shown in **Figure 3I**. When  $\alpha \approx 1$  the major principal stress points along the  $x$ -axis, and when  $\alpha \approx 0$ , the principal stress lies in the  $yz$  plane. For  $x \leq L$  we find that the major principal stress is collinear with the system geometry, and the Janssen stress model fits well. In a traditional silo problem, gravity acts parallel to the applied stress, and averaging across the width of a silo ensures the validity of this assumption. For this case, however, because the direction of gravity has broken the inherent symmetry of the silo problem, its validity is not ensured [20]. We do, however, find that this assumption holds well for this and all simulations reported here.

### 3.1. Gap spacing

As motivated in Equation (6), the gap spacing  $D$  largely controls the magnitude of the stresses within the system. For this reason, we here vary this spacing systematically from  $D = 1$  to  $D = 15$ , while maintaining  $\phi_0 = 0.5 \pm 0.05$  and  $I = 0.01$  (except for the case of  $D = 1$ , where  $\phi_0 \approx 0.66$ ), as depicted for four values of  $D$  in **Figure 5**. To make a reasonable comparison between these simulations, in each case the area of the piston is kept constant, such that its area is  $WD = 100$ . Select measures of the behavior of the system are shown in **Figure 6**. Slope angles,  $\theta$ , are averaged over the times corresponding to  $2D \leq L \leq 10D$ , whilst  $K$  and  $\sigma_T$  are averaged temporally over values in the range  $2D \leq L \leq 10D$ , where at each time we measure spatially in the range  $L/4 \leq x \leq 3L/4$ . In **Figures 6A,B**, we observe increasing solid fraction in the plug,  $v_m$ , and slope angle,  $\theta$ , with increasing gap spacing, as the effect of the boundaries on the system decreases.



For each simulation, the measured normal stress at the piston,  $\sigma_h^p$ , is fitted with Equation (6), and a best fit estimate of  $K_z$  is shown as crosses, with the standard deviation of the error of the regression used as error bars, in **Figure 6C**. The mean and standard deviation of the measured values of  $K_z$  and  $K_y$  from the continuum data between  $L = 2D$  and  $L = 10D$  are shown as dots and triangles, respectively. For  $D \geq 2$  we find that both the measured values of  $K_z$  and  $K_y$  are independent of  $D$ , and have mean values of  $K_y = 0.67 \pm 0.04$  and  $K_z = 0.58 \pm 0.05$ . Best fit estimates of  $K_z$  are also independent of  $D$ , with mean values of  $K_z = 0.56 \pm 0.07$ . **Figure 6D** shows the mean of  $\sigma_T$  also from  $L = 2$  to  $L = 10$ . Triangles represent the prediction from Equation (5) using the measured values of  $v_m$ ,  $\theta$  and  $\phi_0$ . In all cases, we find the measured and fitted values of  $K_z$  to be in agreement, whereas the values of  $\sigma_T$  agree only with  $D \geq 3$ . We note, however, that  $\sigma_T$  depends strongly on  $\theta$ , and we have as yet no means for predicting this quantity. The dependence of  $\sigma_T$  on  $\theta$  is in contrast to studies on fold and thrust belts [21], where there is no confinement vertically above the material.

### 3.2. Initial Packing Fraction

Existing models [8, 9] for the evolution of the stresses in similar geometries have neglected any effect of the initial packing fraction  $\phi_0$ . To test this assumption, we here vary  $\phi_0$  from 0.1 to 0.6, while maintaining  $D = 5$  and  $I = 0.01$ . As shown in **Figures 7A,B**, the packing fraction inside the plug and the slope of the transition zone are independent of the initial packing fraction. In **Figure 7C**, we observe that the measured and best fit values of  $K_z$  are in agreement for a wide range of  $\phi_0$ , and that these values are lower than the measured values of  $K_y$ . The prediction of threshold stress from Equation (5), which includes a dependence on  $\phi_0$ , slightly under-predicts the threshold stress at  $\phi_0 = 0.1$ . Nevertheless, both the measured and predicted values of the threshold stress in **Figure 7D** are in agreement with observations from Eriksen et al. [8], where a non-dimensional threshold stress of  $\sigma_T = 10.7$  was found to reproduce the observed pattern formation behavior in the quasi-static limit, at  $D = 5$ , for a range of values of  $\phi_0 \leq 0.5$ .

### 3.3. Inertial Number

Finally, we wish to comment on inertial effects in such a system. Toward this end we systematically vary the inertial number  $I$

from  $10^{-2}$  to 10 while maintaining  $D = 5$  and  $\phi_0 = 0.5 \pm 0.05$ . As shown in **Figure 8**, a transition occurs at  $I \approx 0.1$ , where the quasistatic behavior begins to be dominated by inertial effects, and the system is fluidized. In **Figure 8A**, we notice a jump in the maximum solid fraction, as the particles begin to flow and rearrange due to the increased piston velocity. This is accompanied by an increase in the slope angle  $\theta$  (**Figure 8B**), and a decrease in the accumulation rate (**Figure 8C**, as the grains begin to slip relative to the walls. With increasing piston velocity, the anisotropy of the system is lost, as shown in **Figure 8D**, and both  $K_y$  and  $K_z$  tend toward a mean value of  $0.56 \pm 0.02$  for  $I \geq 1$ . As shown in **Figure 8E**, the threshold stress,  $\sigma_T$ , also diverges above  $I = 0.1$  away from the theoretical prediction. For values of  $I \geq 0.1$ , we have therefore used the measured value of  $\sigma_T$  in the best fit estimation of  $K_z$  shown in **Figure 8D**, rather than the value predicted from Equation (5), as used in all other cases.

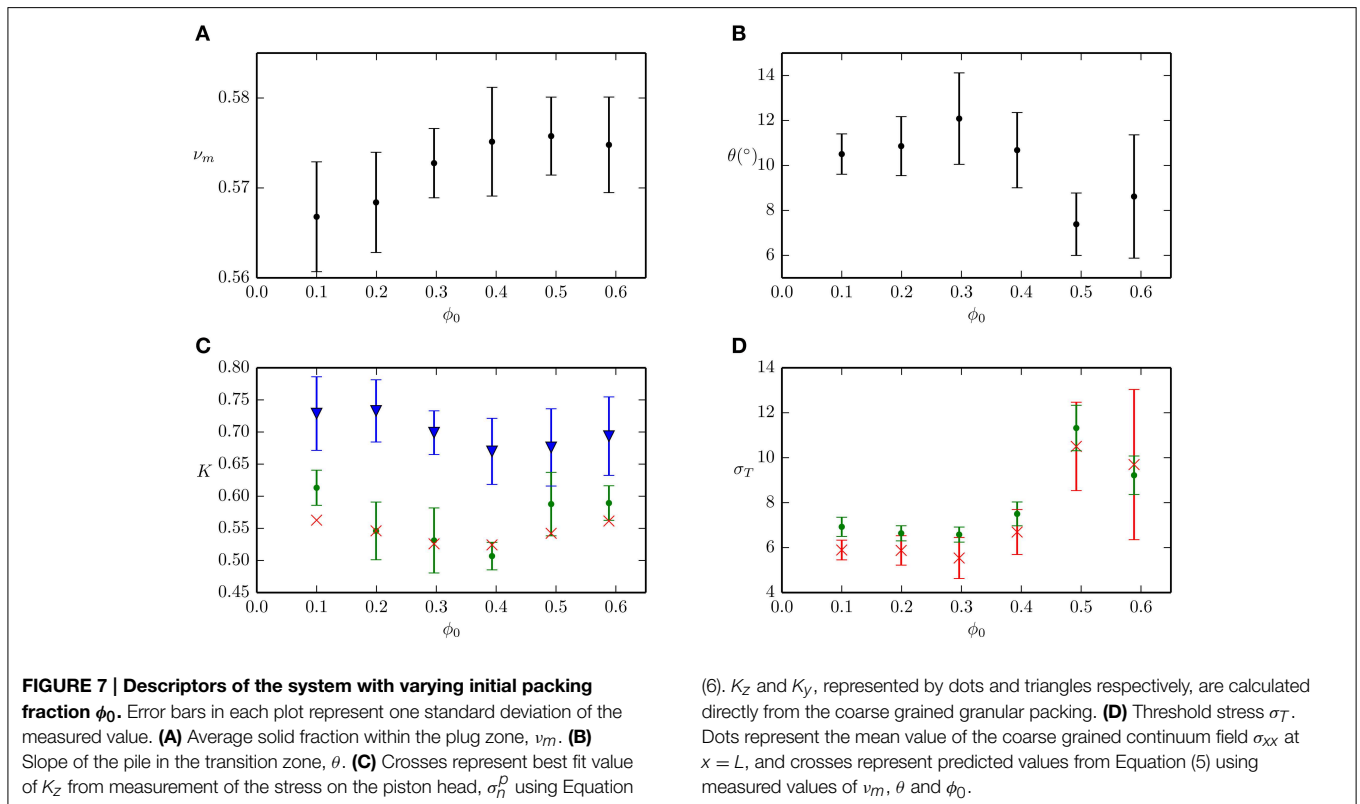
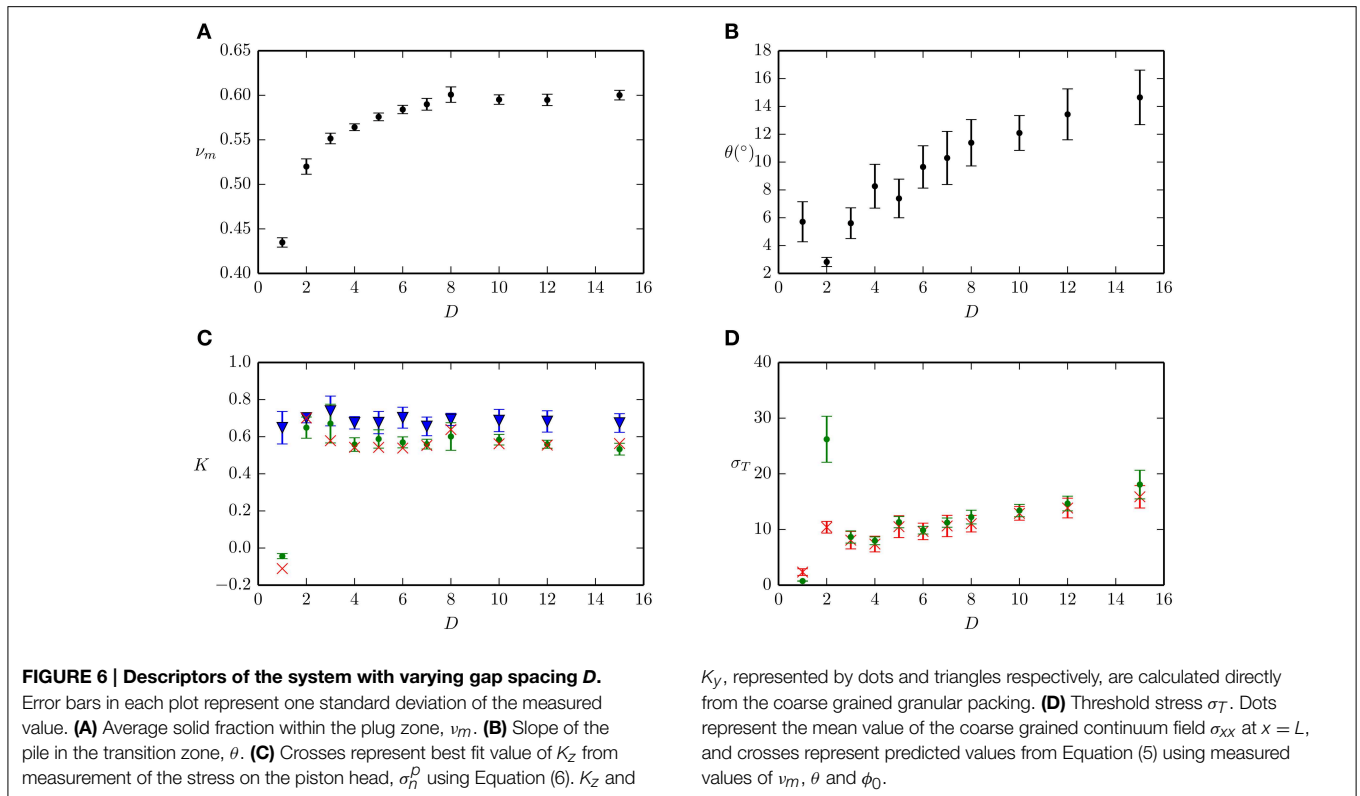
## 4. Conclusions

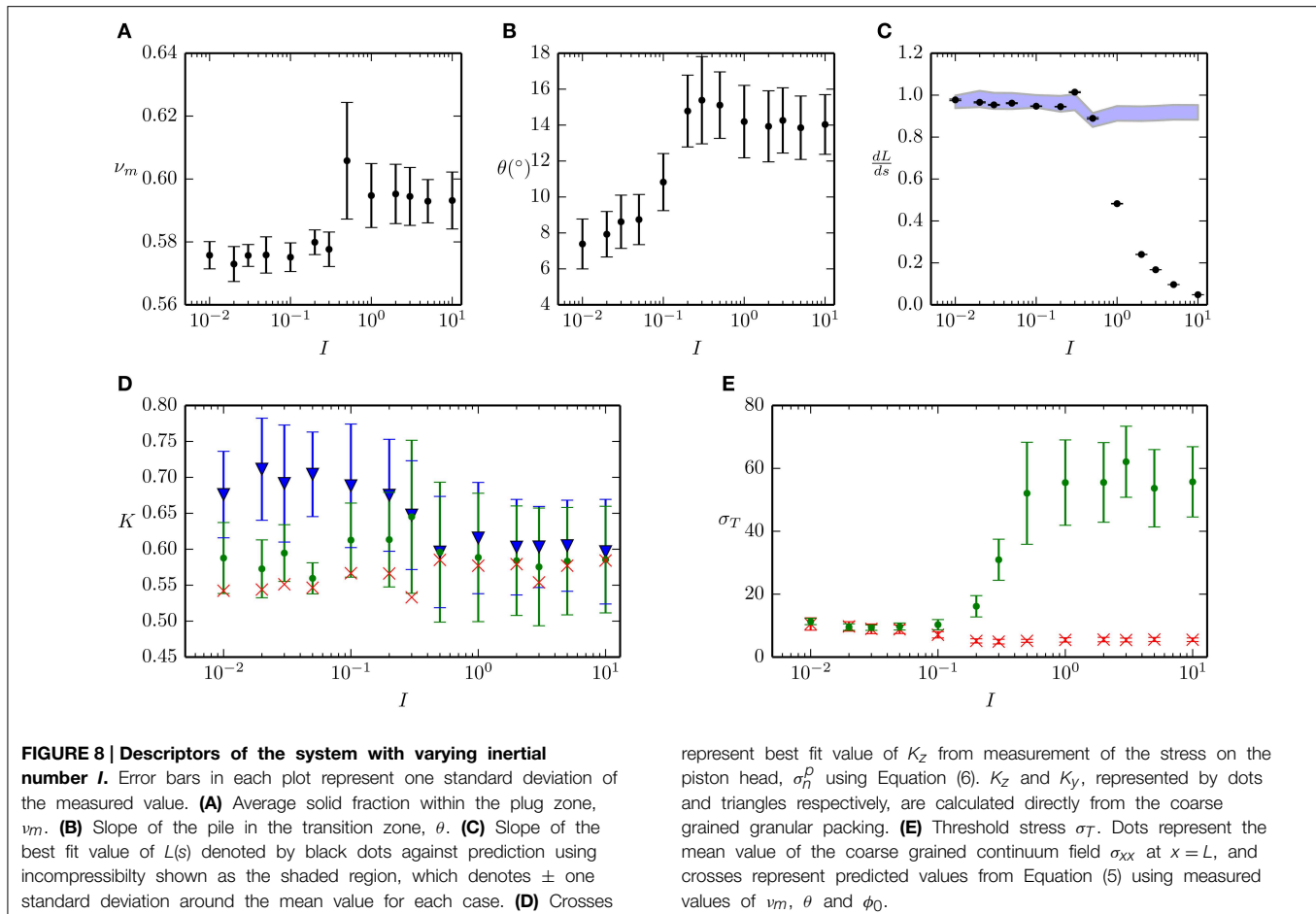
We have here described a large number of simulations of granular materials which have been compacted in a confined geometry. For all cases, we observed that the stress distribution within the packing is well approximated by previous models, once a more rigorous definition of the threshold stress is used. This is true for a wide range of gap spacings, initial filling fractions and piston rates.

In this study we have used a rough boundary condition, where macroscopic friction at the piston and walls is equal to the inter-particle friction. However, in many systems we expect the roughness at the boundaries to be lower than that between particles. It is unclear how this difference will affect either the accumulation of material near the piston head, or the stress distribution within the packing.

Below a gap spacing of 3 particle diameters, the stress distribution is not well represented by this model. We conclude that  $D = 3$  represents the smallest system size which may reasonably be described by the one dimensional Janssen stress model. In addition, at inertial numbers of  $I \geq 0.1$ , we find that there is significant slip at the boundary, and the threshold stress diverges from the model prediction. In all cases, we cannot as yet predict the slope of the free surface in the transition zone, but we observe that this slope approaches the angle of repose for large systems at low piston rates. Janssen stress coefficients for this system are well represented by  $K_z = 0.6 \pm 0.1$  and  $K_y = 0.7 \pm 0.1$  for a wide range of system parameters. A model for the threshold stress has been presented using limit equilibrium, and this holds well for systems with  $D \geq 3$  and  $I < 0.1$ .

The slope angle,  $\theta$ , has been measured for different system parameters to lie in the range of  $2^\circ$ – $18^\circ$ . *A priori*, we could only assume that this angle must be smaller than or equal to the angle of repose, which for these grains is approximately  $20^\circ$ . The wide variability of  $\theta$  is as yet unexplained, and is in contrast to the case where a top boundary does not exist, for example in fold and thrust belts [21], bulldozing [22] and additive manufacturing using loose powders [23]. We do note, however, that at large values of  $D$  the slope angle approaches the angle of repose.





With regards to the two Janssen parameters, we can clearly distinguish the values of  $K_y$  and  $K_z$  in **Figures 6C, 7C, 8D**, for  $I < 0.1$ . The reason for the difference between these two quantities may either be due to anisotropy in the granular packing, or due to the differing boundaries in the  $y$  and  $z$  directions. As the Janssen parameters are relatively insensitive to the gap spacing  $D$ , we conclude that this anisotropy is due to the accumulation process, which creates a preferential direction within the packing. This distinction is important when considering models which account for more complex geometries, such as in Eriksen et al. [8]. For industrial applications, such as propped fractures or sand production, the stresses within a plug of grains in a horizontal crack are expected to be a function not only of the relative size of the grains to

the crack width, but also the rate of accumulation of the grains.

## Author Contributions

BM conducted the simulations, post-processing and authored the paper. BS conceived the idea for the simulations. BS, GD, JE, and KM assisted with the interpretation and analysis of the simulations, and editing of the manuscript.

## Acknowledgment

The authors would like to acknowledge grants 213462/F20 and 200041/S60 from the NFR.

## References

- Bräuer K, Pfitzner M, Krimer DO, Mayer M, Jiang Y, Liu M. Granular elasticity: stress distributions in silos and under point loads. *Phys Rev E* (2006) **74**:061311. doi: 10.1103/PhysRevE.74.061311
- Landry JW, Grest GS, Silbert LE, Plimpton SJ. Confined granular packings: structure, stress, and forces. *Phys Rev E* (2003) **67**:041303. doi: 10.1103/PhysRevE.67.041303
- Sperl M. Experiments on corn pressure in silo cells—translation and comment of Janssen's paper from 1895. *Granular Matter* (2006) **8**:59–65. doi: 10.1007/s10035-005-0224-z
- Janssen HA. Versuche über getreidedruck in silozellen. *Zeitschr d Vereines Deutscher Ingenieure* (1895) **39**:1045–9.
- Tronvoll J, Fjaer E. Experimental study of sand production from perforation cavities. *Int J Rock Mech Mining Sci Geomech Abstr.* (1994) **31**:393–410. doi: 10.1016/0148-9062(94)90144-9



6. Veeken CAM, Davies DR, Kenter CJ, Kooijman AP. Sand production prediction review: developing an integrated approach. In: *SPE Annual Technical Conference and Exhibition*. Society of Petroleum Engineers. Dallas, TX, (1991). p. 335–46.
  7. Milton-Taylor D, Stephenson C, Asgjan MI. Factors affecting the stability of proppant in propped fractures: results of a laboratory study. In: *SPE Annual Technical Conference and Exhibition*. Society of Petroleum Engineers. Dallas, TX, (1992). p. 569–79.
  8. Eriksen JA, Marks B, Sandnes B, Toussaint R. Bubbles breaking the wall: two-dimensional stress and stability analysis. *Phys. Rev. E*. (2015) **91**:052204. doi: 10.1103/PhysRevE.91.052204
  9. Knudsen HA, Sandnes B, Flekkøy EG, Måløy KJ. Granular labyrinth structures in confined geometries. *Phys Rev E*. (2008) **77**:021301. doi: 10.1103/PhysRevE.77.021301
  10. Sandnes B, Flekkøy EG, Knudsen HA, Måløy KJ, See H. Patterns and flow in frictional fluid dynamics. *Nat Commun*. (2011) **2**:288. doi: 10.1038/ncomms1289
  11. Sandnes B, Knudsen HA, Måløy KJ, Flekkøy EG. Labyrinth patterns in confined granular-fluid systems. *Phys Rev Lett*. (2007) **99**:038001. doi: 10.1103/PhysRevLett.99.038001
  12. Bratberg I, Måløy KJ, Hansen A. Validity of the Janssen law in narrow granular columns. *Eur Phys J E* (2005) **18**:245–52. doi: 10.1140/epje/e2005-00030-1
  13. Thornton AR, Weinhart T, Luding S, Bokhove O. Modeling of particle size segregation: calibration using the discrete particle method. *Int J Modern Phys C* (2012) **23**:1240014. doi: 10.1142/S0129183112400141
  14. Weinhart T, Thornton AR, Luding S, Bokhove O. From discrete particles to continuum fields near a boundary. *Granular Matter*. (2012) **14**:289–94. doi: 10.1007/s10035-012-0317-4
  15. Luding S. Cohesive, frictional powders: contact models for tension. *Granular Matter* (2008) **10**:235–46. doi: 10.1007/s10035-008-0099-x
  16. Fuchs R, Weinhart T, Meyer J, Zhuang H, Staedler T, Jiang X, et al. Rolling, sliding and torsion of micron-sized silica particles: experimental, numerical and theoretical analysis. *Granular Matter* (2014) **16**:281–97. doi: 10.1007/s10035-014-0481-9
  17. GDR MiDiA. On dense granular flows. *Eur Phys J E* (2004) **14**:341–65. doi: 10.1140/epje/i2003-10153-0
  18. Goldhirsch I. Stress, stress asymmetry and couple stress: from discrete particles to continuous fields. *Granular Matter* (2010) **12**:239–52. doi: 10.1007/s10035-010-0181-z
  19. Weinhart T, Hartkamp R, Thornton AR, Luding S. Coarse-grained local and objective continuum description of three-dimensional granular flows down an inclined surface. *Phys Fluids* (2013) **25**:070605. doi: 10.1063/1.4812809
  20. Nedderman RM. *Statics and Kinematics of Granular Materials*. Cambridge: Cambridge University Press (2005).
  21. Davis D, Suppe J, Dahlen FA. Mechanics of fold-and-thrust belts and accretionary wedges. *J Geophys Res*. (1983) **88**:1153–72. doi: 10.1029/JB088iB02p01153
  22. Sauret A, Balmforth NJ, Caulfield CP, McElwaine JN. Bulldozing of granular material. *J Fluid Mech*. (2014) **748**:143–74. doi: 10.1017/jfm.2014.181
  23. Parteli EJR. DEM simulation of particles of complex shapes using the multisphere method: application for additive manufacturing. *AIP Conf Proc*. (2013) **1542**:185–8. doi: 10.1063/1.4811898
- Conflict of Interest Statement:** The authors declare that the research was conducted in the absence of any commercial or financial relationships that could be construed as a potential conflict of interest.
- Copyright © 2015 Marks, Sandnes, Dumazer, Eriksen and Måløy. This is an open-access article distributed under the terms of the Creative Commons Attribution License (CC BY). The use, distribution or reproduction in other forums is permitted, provided the original author(s) or licensor are credited and that the original publication in this journal is cited, in accordance with accepted academic practice. No use, distribution or reproduction is permitted which does not comply with these terms.*